Check for updates

Characterizing dark state kinetics and single molecule fluorescence of FusionRed and FusionRed-MQ at low irradiances†

Srijit Mukherjee, [ab] Connor Thomas, [a] Ryan Wilson, [ac] Emma Simmerman, [d] Sheng-Ting Hung *[e] and Ralph Jimenez *[ab]

The presence of dark states causes fluorescence intermittency of single molecules due to transitions between ''on'' and ''off'' states. Genetically encodable markers such as fluorescent proteins (FPs) exhibit dark states that make several super-resolved single-molecule localization microscopy (SMLM) methods possible. However, studies quantifying the timescales and nature of dark state behavior for commonly used FPs under conditions typical of widefield and total internal reflection fluorescence (TIRF) microscopy remain scarce and pre-date many new SMLM techniques. FusionRed is a relatively bright red FP exhibiting fluorescence intermittency and has thus been identified as a potential candidate for SMLM. We herein characterize the rates for dark-state conversion and the subsequent ground-state recovery of FusionRed and its 2.5-fold brighter descendent FusionRed L175M M42Q (FusionRed-MQ) at low irradiances (1–10 W cm^{-2}), which were previously unexplored experimental conditions. We characterized the kinetics of dark state transitions in these two FPs by using single molecule blinking and ensemble photobleaching experiments bridged with a dark state kinetic model. We find that at low irradiances, the recovery process to the ground state is minimally light-driven and FusionRed-MQ has a 1.3-fold longer ground state recovery time indicating a conformationally restricted dark-state chromophore in comparison to FusionRed. Our studies indicate that the brighter FusionRed-MQ variant exhibits higher dark state conversion rates with longer ground state recovery lifetimes, thus it is potentially a better candidate for SMLM applications than its progenitor FusionRed.

Introduction

Fluorescence-based bioimaging and biosensing, such as multi-color microscopy, Förster resonance energy transfer (FRET) and fluorescence lifetime imaging microscopy (FLIM), is the primary non-invasive approach to image biological systems.[1–6]

a JILA, University of Colorado, Boulder and National Institute of Standards and Technology, 440 UCB, Boulder, Colorado 80309, USA. E-mail: rjimenez@jila.colorado.edu

b Department of Chemistry, University of Colorado, Boulder, 215 UCB, Boulder, Colorado 80309, USA

c Department of Physics, University of Colorado, Boulder, 390 UCB, Boulder, Colorado, 80309, USA

d Department of Applied Physics, Stanford University, 348 Via Pueblo Mall, Stanford, CA 94305-4090, USA

e Department of Physics, National Sun Yat-sen University, Kaohsiung 80424, Taiwan. E-mail: sth@mail.nsysu.edu.tw

† Electronic supplementary information (ESI) available: Sections S1 to S9 have been provided to support certain results and techniques used in the manuscript. Spot Identification, trajectory binarization, Monte–Carlo simulations and single molecule analysis codes are available on GitHub: https://github.com/srijit2207/FR_DarkState.git. See DOI: https://doi.org/10.1039/d2cp00889k

Due to Abbe's diffraction limit, imaging sub-wavelength biological substructures requires innovations beyond the scope of conventional microscopy.[7] Probing this "super-resolution" scale has high value to modern biology and has garnered the attention of scientists and engineers from a range of specializations – making it a popular interdisciplinary field of research and development.[8–13] Techniques like stimulated emission depletion microscopy (STED), photoactivated localization microscopy (PALM), reversible saturable optical fluorescence transition microscopy (RESOLFT), and other single-molecule localization microscopy (SMLM) overcome Abbe's limit through biochemical or optical modulation of single emitters.[14–17] Most SMLM methods, including single-molecule active control microscopy (SMACM), bleaching/blinking assisted localization microscopy (BALM) and super-resolution optical fluctuation imaging (SOFI), rely on photo-activatable or photo-switchable emitters.[16] These emitters can be activated and/or converted to a new species upon irradiation, exhibiting either molecular binding/modification or spontaneous stochastic blinking.[18–22] Techniques that exploit stochastic blinking, such as SOFI, rely on post-processed data analysis algorithms where traditionally acquired fluorescence

time-lapse images are analyzed to obtain spatio-temporal correlations for stochastic fluctuations during emission.[18] Current efforts in this domain focus on application-based analysis of such methods and molecular interpretation of the blinking process for different emitters. A majority of the literature treats emitters simply as tools, with limited analysis of their dark state kinetics and photophysics.[23–25] Unwanted artefacts in the determination of spatial locations for these emitters can thus arise, as a major assumption underlying such stochastic methods is that the signals from single fluorophores are additive as long as the fluorescence dynamics of the molecules are independent.[25]

Fluorescent proteins (FPs) are popular tools for imaging biological systems and are known to exhibit non-fluorescent or "dark" molecular states.[26–30] These dark states are long-lived electronic or conformational states ($>\mu$s) of the FP chromophore. Access to these states limits the participation of a fluorophore in multiple cycles of the faster (ns) S_0–S_1 fluorescence cycle. Trapping of molecules in these semi-permanent non-fluorescent states results in blinking on the single molecule level and reversible dimming at the ensemble level.[26–30] Extensive mechanistic studies have elucidated a diverse range of mechanisms and timescales for stochastic and tuned dark-state conversion, including electron-transfer reactions, excited-state proton transfer, chromophore and, sidechain conformational changes. For example, a number of proteins from the avGFP line display a spontaneous, light-driven, pH-dependent dark-state conversion pathway.[31–33] In such cases a pH-dependent dark state conversion is often attributed to a proton transfer between amino acid residues and the chromophore. The red FP (RFP) DsRed exhibits a similar light-driven dark-state conversion through a different, pH-independent process.[32] Photoconvertible FPs (PCFPs) like IrisFP, mEosFP and Dendra derivatives exhibit dark-state conversion *via* chromophore distortions due to side-chain conformational changes, chromophore twisting motions or by proton transfer from the triplet or a radical ground state.[34–38] Selectively engineered photo-switchable or reversibly-switchable fluorescent proteins (rsFPs) exhibit highly efficient transfer to the dark states, allowing the molecules to be switched on and off with either light-driven pH-dependent pathways or reversible chromophore conformational changes such as a *cis–trans* isomerization along the methylidine bridge connecting the two conjugated rings in the chromophore moiety.[39–41] Dark states can be selectively accessed or depopulated using optical or thermal modulation.[42–48] For example, pulsed excitation with resonant frequencies was used to populate and depopulate the dark state in FPs like AcGFP and rsFastLime, providing selective modulation of fluorescence.[45] Varied mechanisms of accessing dark states as listed above have made FPs natural choices for several SMLM techniques.

Despite the extensive advances in the study of dark-state dynamics, many of the above-mentioned studies far preceded the development of advanced SMLM techniques such as SOFI. Several previous studies were constrained by experimental challenges to probing dark state dynamics with irradiances on the order of kW cm^{-2} to attain adequate signal to noise ratios.[26–32] While these studies explore the fundamentals of

dark states in FPs, probing dark-state dynamics at high irradiances comes with a three-fold disadvantage. These conditions accelerate permanent photodegradation of the fluorophore, make extrapolation to much lower irradiance as in widefield and SMLM regimes difficult, and cause light-induced phototoxicity and photodamage to biological systems.[18,49,50] It is also worth noting that blue shifting the excitation light increases phototoxicity, thus highlighting the need for development of new bright and red-shifted fluorophores as well as for detailed photophysical characterization of existing red fluorophores – which additionally allow for deeper imaging in comparison to blue shifted analogues.[50,51] When extrapolating the rate constant of ground-state recovery (k_{GSR}) to low irradiances from high irradiance measurements, k_{GSR} is commonly assumed to be proportional to the excitation rate (k_{Ex}).[28,52] Often, the recovery from a dark to a fluorescent state is often a consequence of conformational switching such as a dark-*trans* to fluorescent-*cis* isomerization of the FP chromophore.[53] Since such conformational switches are often energetically controlled, the excitation dependence of k_{GSR} may originate from the absorption of the excitation photons by dark state species and/or the rise of local temperature due at higher irradiances.[28,52,54]

FusionRed and its sibling TagRFP-T exhibit fluorescence intermittency in live-cell imaging using TIRF microscopy with camera acquisition timescales of 50 ms.[55] Klementieva and coworkers demonstrated the potential to achieve a theoretical spatial resolution beyond the diffraction limit ($\sim$25–30 nm) with FusionRed using SMLM methods like BALM and SOFI.[55] In our previous work, we developed FusionRed-MQV, a FusionRed variant with 3-fold higher molecular brightness developed using a combination of lifetime-based microfluidic selection and site-directed mutagenesis.[53] Additionally, we found that the substitution C159V in FusionRed resulted in a brighter variant which showed a monoexponential photobleaching trace contrary to the biexponential behavior exhibited by the parental RFP FusionRed. Variants lacking the C159V substitution, like the 2.5-fold brighter FusionRed-MQ exhibited biexponential photobleaching traces with a fast fluorescence decay component ($\sim$s) followed by a significantly slower decay component ($>$100 s).[53] The faster component was attributed to reversible photobleaching, where fluorescent molecules are trapped in the dark state.[53] This was verified by employing a high-energy 438 nm pulse ($\sim$2 s; 50% duty) with a continuous 560 nm excitation scheme which resulted in distinct reversible photoswitching for FusionRed variants with a Cys residue at position 159.[53] High energy 438 nm light prompts a return to the fluorescent state from a dark state, suggesting that the lower energy 560 nm excitation minimally perturbs the ground state recovery process.[53] Together with findings and from other studies, including crystal structure data, the interconversion of the FusionRed chromophore from a fluorescent *cis* to a dark *trans* isomer is a plausible mechanism for photoswitching.[56,57] Moreover, in the low irradiance regime of 1–10 W cm^{-2}, the temperature increase in the vicinity of an FP molecule can be considered negligible – indicating minimal light driven recovery of fluorescent fractions from dark states.[58] Based on these

This journal is © the Owner Societies 2022

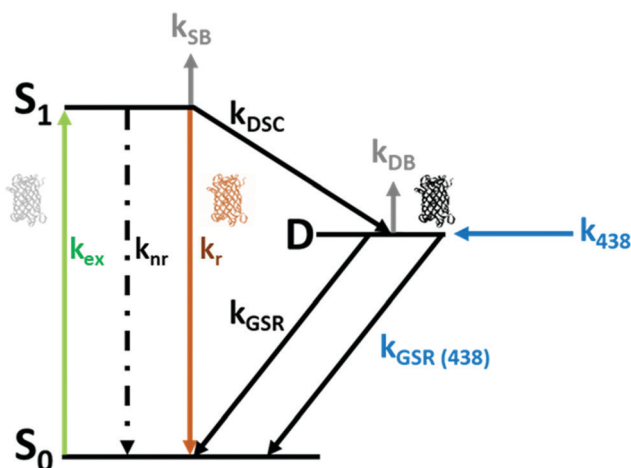*Phys. Chem. Chem. Phys.*, 2022, **24**, 14310–14323 | **14311**

Fig. 1 A three-state model of the photophysics of a fluorophore central to this study. The 561 nm excitation source allows access to the excited electronic (S$_1$) state from the ground electronic (S$_0$) state. Following this, the fluorophore can either return to S$_0$ or access a long lived dark (D) state. The molecule can consequently return to the fluorescent S$_1$-S$_0$ cycle with the ground-state recovery pathway (k_{GSR}). It was demonstrated in our previous work that the D can be depopulated efficiently using a 438 nm light (k_{438} for the rate constant of irradiation with corresponding $k_{GSR\ (438)}$).[53] The arrow labels k_{Ex}, k_{nr}, k_r, k_{DSC} and k_{GSR} indicate the rate constants for excitation, non-radiative decay (internal conversion), radiative emission, S$_1$ to dark state conversion and dark state to S$_0$ recovery, respectively. Rate constants of permanent photobleaching from the S$_1$ (k_{SB}) and the D (k_{DB}), represented with grey arrows, are ignored in the low irradiance regime.

observations, we hypothesized that the rate of recovery to the ground state (k_{GSR}) is independent of the excitation rate (k_{Ex}) for FusionRed and FusionRed-MQ. To verify these claims, we explore the relatively uncharted territory of dark state kinetics of these two RFPs under low irradiances, central to widefield and SMLM techniques like SOFI. By extracting on–off statistics with single molecule imaging and exploiting the kinetics of reversible photobleaching using widefield excitation on ensemble RFPs, we combine the strength of each approach to quantitatively extract rate constants of dark-state conversion (k_{DSC}) and ground-state recovery (k_{GSR}) using a three-state model (Fig. 1). We performed simulations utilizing Monte Carlo methods to bridge the two extremes in imaging modalities and qualitatively validate the three-state model. Finally, we propose a structural model to rationalize the dark-state dynamics observed for these FPs.

Methods

Experimental methods and data collection

Cell growth and protein purification. FusionRed and FusionRed-MQ in the pBad-His plasmid DNA were transformed into *E. coli* (Top10 strain) *via* heat shock and grown for 45–60 minutes in LB media at 37 °C and 230 rpm.[53] The transformants were plated on agar plates with 100 μg mL^{-1} ampicillin and 0.2% arabinose (Sigma Aldrich) overnight at 37 °C. Colored colonies were grown in 200 mL 2XYT (VWR) liquid cultures with 100 μg mL^{-1} ampicillin for 1–3 hours at 37 °C and 230 rpm to

an OD of 0.6. Arabinose was then added (0.2%) to induce protein expression for 16–24 hours at 28 °C and 230 rpm. The cells were pelleted, chemically lysed (B-PER, Thermo Fisher Scientific) and the 6-His tagged FPs were isolated on Ni-NTA columns (Thermo Fisher Scientific) by gravity filtration, eluting with 250 mM imidazole (Sigma Aldrich). Excess imidazole was removed with desalting columns (GE Healthcare) with dialysis buffer (150 mM NaCl, 50 mM Tris–HCL, pH 7.4) as an eluent.

Single molecule measurements

Preparation of glass slides and coverslips. Minimizing the presence of fluorescent impurities is of particular concern in single-molecule studies. To reduce artefacts from impurities in our measurements, we found that plasma-cleaned glass slide chambers were best suited to single molecule TIRF.[59] Before plasma cleaning, the slides and coverslips (22 × 40 mm, No. 1, VWR) were cleaned with dilute HCl then washed with Alconox detergent and rinsed with deionized water, then soaked in methanol overnight to dislodge large contaminants. A custom aluminum slide holder held the slides and coverslips inside a reactive ion etcher, such that both sides were exposed to the plasma. The slides were then exposed to 300 s of O$_2$ (Bias: 50 W and SCCM: 50 mTorr) plasma to remove organic contaminants and to charge their surfaces, followed by 60 s of Ar plasma (Bias: 50 W and SCCM: 50 mTorr) to minimize presence of remaining reactive oxygen species. The slides were used within 24 hours after plasma cleaning to avoid recontamination and loss of surface charge.

Sample preparation. The pure protein samples were diluted with Tris-HCl buffer (pH ∼ 7.4–8.0) and loaded by slow ejection from a 200 μL micropipette. It was determined that FP concentrations > 300 pM caused crowding of FPs in the field of view and failure of our spot analysis algorithm to report blinking trajectories, whereas concentrations < 100 pM resulted in such sparse distribution that it became difficult to find the correct focus height and provided few data points. Additionally, a washing procedure was developed to minimize the presence of non-adhered FPs in solution and thus minimize free FP diffusion into the imaging plane. The loaded chamber was left in the dark for 10–15 minutes to allow FPs to settle onto the imaging surface, then a volume of imaging buffer (150 mM HEPES, 100 mM NaCl, pH 7.4) equal to the volume of the loaded sample was passed through the chamber 4–6 times, with 2 minute intervals between washes. The liquid was slowly ejected by a micropipette on one side of the chamber while filter paper was used to absorb the liquid flowing out from the other side. This washing procedure helped to maximize signal-to-background ratios and minimize artifacts from non-specific adhesion to the glass surface for FPs in solution.

TIRF imaging. The samples were imaged with TIRF microscopy on an Olympus IX-73 inverted microscope. The microscope was accessorized with an Olympus cellTIRF-1Line system fiber coupled to a laser (Toptica iChrome MLE). An Olympus 60×-in-oil (NA:1.42) TIRF objective and an EMCCD camera (Andor iXon 897) were used for the single molecule experiments. A schematic of this system has been provided in ESI,†

14312 | *Phys. Chem. Chem. Phys.*, 2022, **24**, 14310–14323

This journal is © the Owner Societies 2022

Section S1 and Fig. S1.1. To measure the excitation rate, the objective focus was first determined by imaging a dye sample under bright-field illumination, then the sample was removed and the laser was focused at the ceiling (approximately 2 m beyond the sample location) for this z-position of the objective. The irradiance measurements were carried in this normal (I_{Normal}) to the imaging plane position using a power meter (X-cite). The excitation intensity of the evanescent field (I_{TIRF}) was calculated from the incident intensity (I_{Normal}), the indices of refraction (η_2, η_1), and the incident angle.[60] The calculations of excitation rates for normal and TIRF illumination are presented in ESI,† Fig. S2. To image samples, a cropped area of the imaging plane ($\sim 128 \times 128$ pixels on a 256×256-pixel binning) corresponding to the region of highest intensity of the laser profile was selected. For the lowest value of irradiance (~ 1 W cm^{-2}), 100 nm fluorescent beads (TetraSpeck) were used to first determine the approximate z-focus, and the motorized stage (Prior) was moved in the x–y plane to the position of single FP molecules, to determine an accurate focus. The experiment was started after moving to an adjacent spot (~ 100 μm) outside this imaging area of the previous step, where drift on the z-axis was minimal. This was done to minimize photobleaching of single molecules.

Ensemble measurements

Bright bacterial colonies on the agar plates described above were chosen for time-lapse photobleaching experiments. Two to three colonies were transferred to microcentrifuge tubes and washed with 500 μL imaging buffer by vortexing for ~ 20 s. The cells were centrifuged at 3000–5000 RPM for 60 s, and the washing buffer was removed. The pelleted cells were then resuspended in the same buffer to an OD in the range of 0.1 to 0.5 to get a cell density suitable for imaging. A glass coverslip and slide were cleaned with Alconox detergent, rinsed with deionized water, and blown dry with filtered compressed air. 10–20 μL of the cell mixture was added between the coverslip and slide, which was imaged on an Olympus IX-73 inverted microscope system. Samples were excited by 560 nm continuous wave LED illumination (Lumencor). Fluorescence bleaching measurements were taken with the 20× or 40×-in air objective lens (Olympus). The fluorescence was collected through a 629/56 nm band-pass filter by a SCMOS camera (Andor Zyla). Videos were collected with 10–50 ms exposure times and frame rates of 20–32 FPS for the fast and reversible component of the decay and 10–20 FPS for the slow and irreversible component, and with irradiances ranging from 1–20 W cm^{-2}. We performed three independent trials where each trial for an FP involved a technical replicate with ~ 10–20 cells to gain consistent bleaching traces.

Data analysis

Single molecule data analysis. Single molecule data analyses from imaging videos were carried out using two independent scripts: One for spatial identification of bright spots followed by one for temporal and intensity analysis of these bright spots. Fig. 2 shows a schematic representation of this workflow.

Spot identification script. Despite cropping, there is a systematic $\sim 10\%$ intensity variation across the imaging plane with a Gaussian profile. To account for this, the videos were iteratively fitted to a Gaussian intensity correction function to
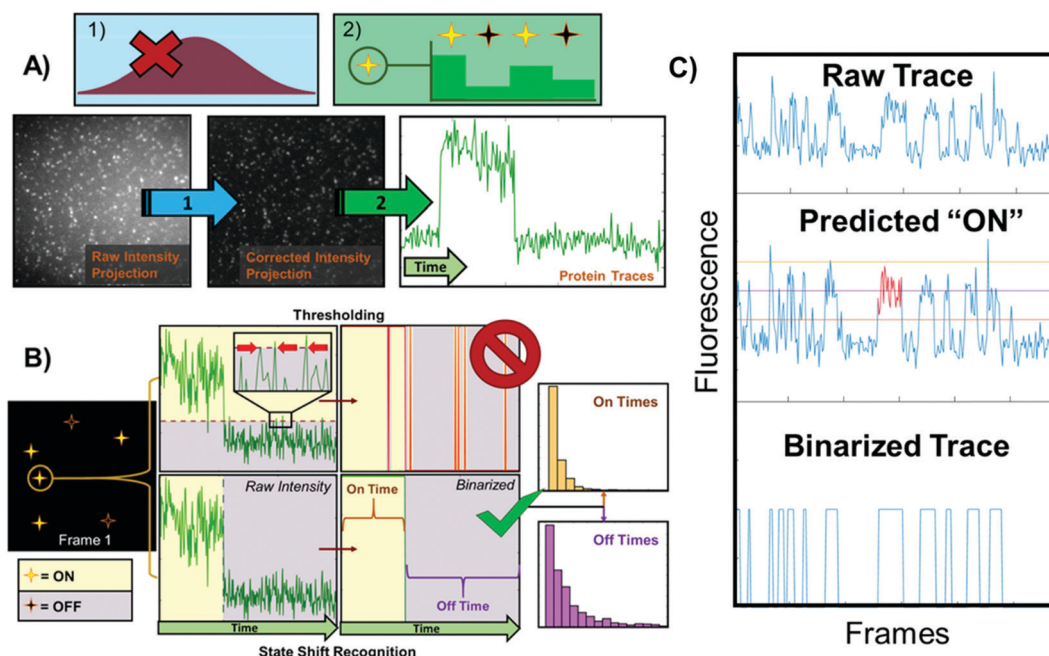

Fig. 2 Analysis workflow. (A) The background correction and molecule selection. (B) Our analysis workflow contrasted against standard thresholding methods. Note that the state shift recognition workflow identifies points where possible changes occur and binarizes on the basis of those points. This avoids the noise-based artifacts shown in the thresholding approach, where it can be difficult to set an arbitrary threshold that is not crossed by noise. (C) The binarization of a raw trace based on the thresholding algorithm.

This journal is © the Owner Societies 2022

Phys. Chem. Chem. Phys., 2022, **24**, 14310–14323 | **14313**

correct for the laser background, primarily from residual scattering, and normalizing for the variation in intensity due to the spatial mode of the excitation laser. (ESI,† Section S3 and Fig. S3.1) Following Gaussian correction, our analysis also revealed a biexponential decay of mean intensities across the timeframe of the video. Therefore, the mean intensity of the videos was fitted to a biexponential function, which revealed a fast component of decay (~ 1 s) along with a slow component of decay (>3 s). While the timescale of the slow component of decay varied with the incident intensity, the fast component was seen to be fairly consistent (ESI,† Section S3 and Fig. S3.1c). Additional checks with blank solutions also revealed a consistent timescale for the fast component of decay. Therefore, after the Gaussian correction, a secondary correction was incorporated to account for the quick exponential drop in the overall light intensity. Given that this decay was also found in blank medium and was missing from the laser's temporal profile, we attribute it to diffusion or photobleaching of impurities in our blank medium or the objective oil. Following the Gaussian and exponential corrections, the algorithm identifies a number of bright locations equal to an input of the predicted number of single FPs in the video. This number was set between 50 and 500 FPs depending on the field of view, the efficiency of binding the FPs to the glass surface and the concentration of the protein used. The algorithm extracts the brightest pixels in the maximum intensity projected image of the video from the user defined input value for the number of single FPs. It then iteratively appends the location of maximum value after it passes a check, which involves scanning a pixel grid surrounding the pixel centered at maximum value based on the statistical distribution of the brightness around the grid.

Temporal and intensity analysis. To extract information on real "on" and "off" blinking events we drew inspiration from the work of Watkins and Yang.[61] In order to find on and off time segments in the time trajectory of a single molecule, we used an intensity change point approach. Our spot analysis script provides us with intensity corrected trajectories for the brightest spots arranged in the ascending order of mean intensity. We therefore assessed the first five and the last five trajectories, based on the brightest and the dimmest spots identified through the previous script. In each case, we estimated the average single molecule on intensity to provide as an input for this code. Although many approaches utilize histograms from the intensities of each frame to effectively threshold and binarize a trajectory, it is difficult to use this approach for our data sets at the lower and the upper bounds of irradiances, which are characterized by increasingly longer on or off time segments, respectively.[62]

Following the input of the five potential on events, our algorithm performs two steps. First, it fits the change of intensity between frames for the entire dataset to a Gaussian distribution. It should be noted that a protein turning on or off produces a relatively small change in intensity that falls within the noise distribution. Therefore, it is not possible to separate these events from background noise with equal or higher intensity *a priori*, but appropriate placement of a threshold can allow for the discarding of noise below the threshold value.

As a result, all frames with a change value of the threshold or higher are earmarked as possible changes of state. Thus, the primary question is where to set the threshold for optimal recognition. (ESI,† Section S3b and Fig. S3.2) The theoretical minimum intensity changes for a molecule results from a case where the protein turns on exactly halfway through a frame's acquisition time. This results in a change of intensity of 1/2 the protein intensity signal, followed by a second change of the same magnitude. As such, a good baseline estimate for the noise threshold value is 50% of the expected signal. Empirically, we have found that $\sim 1.5\ \sigma$ (standard deviation) of the overall noise produced consistent results. This boundary excludes 86% of overall noise, but it is worth noting that the on state contributes to higher (shot) noise. As such, this boundary excludes approximately 70% of the larger standard deviation on distribution. The second step of the algorithm considers the intervals between each on and off point individually and binarizes each segment on the basis of a user-defined "on" segment. (ESI,† Fig. S3.2 and Fig. 2C) This further minimizes the contributions of noise by averaging each segment. Segments that are more than 2σ above the model "on" segment are considered multi-molecule events and the corresponding trace is discarded. All segments that end at the last frame of the video (on or off) are also discarded to avoid artifacts, notably from permanent photobleaching or denaturation. In conclusion, histograms were created using the binning of on and off time segments from the examined trajectories. The average on and off lifetimes (τ_{ON} and τ_{OFF}, described in ESI,† Sections S5a–e) were extracted by fitting the histograms to a probability density function with exponential distributions.

Ensemble data analysis

Photobleaching data analysis was carried out with a previously reported scheme.[53] In brief, a pipeline in the CellProfiler suite[63] was used to identify bacteria in an imaging plane of uniform irradiance and provide normalized intensity trajectories. The intensity trajectories were analyzed and fit to biexponential traces using a custom fitting program in MATLAB (ESI,† Section S4 and Table S4.1).

Results

Single molecule photophysics

Simulations. We simulated single FP blinking trajectories using the three-state (S_0, S_1 and D) model shown in Fig. 1. A schematic of the simulation scheme is presented in Fig. 3 and additional details of the algorithm with simulated tests are described in the ESI,† Section S5. In brief, the residence of single FPs in each state (S_0, S_1 or D) at each time step is simulated using a combination of Monte Carlo methods weighted by the average probabilities of state change. The state change probabilities are governed by the rate constants k_{Ex}, k_r, k_{nr}, k_{DSC} and k_{GSR}, as demonstrated in Fig. 1. While the k_{Ex}, k_r and k_{nr} can be accurately calculated from the measured values of irradiance, extinction coefficient, spectra, quantum yield and
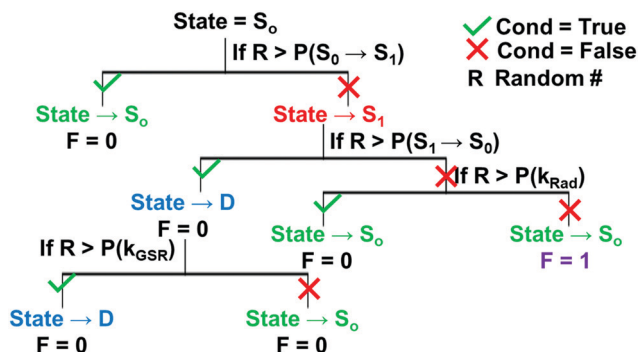
Fig. 3 Schematic representing the algorithm used to simulate single molecule behavior for a three (S_0 = Ground electronic, S_1 = First excited and D = Dark) state model. The value of $F = 1$ indicates a fluorescence photon has been generated in the process, while $F = 0$ indicates a non-fluorescent event.

fluorescence lifetime,[53] k_{DSC} and k_{GSR} required estimates from our experiments and previous works.[64] Based on these results, the k_{DSC} was assumed to be $\sim 10^2$–10^4-fold faster than the k_{GSR}.[64] Using this scheme an "on" or a fluorescent event is detected every time the molecule successfully completes an S_0–S_1–S_0 cycle, without going through D, whereas an off event takes place when the molecule successfully enters the dark state from S_0 through S_1. (Fig. 1 and 3) Additionally, the generated single molecule blinking trajectories from these simulations were utilized to assess the rigor of our temporal and intensity analysis codes for experimental data, described in the methods section.

The simulations suggest that τ_{ON} decreases with both shorter values of τ_{DSC} and higher values of k_{Ex}, whereas τ_{OFF} depends only on the value of τ_{GSR}. (ESI,† Section S5a) Furthermore, the algorithm predicts that the observed τ_{ON} and τ_{OFF} observed on a camera are independent of the frame rate (provided frame rate $< k_{GSR}$) and the time-step used for the simulation. (ESI,† Section S5b–d) Commercial cameras that can spatially resolve single molecules are therefore capable of providing molecular insights into the dark state conversion and ground state recovery processes at low irradiances.

Experiments. The irradiances for the laser output values were measured at normal illumination, then single molecule measurements were carried out at these values under TIRF illumination. (ESI,† Section S2) Consequently, the calculated value of excitation rate for the FPs is determined by multiplying

the calculated TIRF irradiance on the sample with the absorption cross section (σ) at the excitation wavelength. ($\sigma_{FR-MQ} \sim 1.7\sigma_{FR}$ at 561 nm) Thus, these measurements were carried out with irradiation on the order of $\sim 10^3$ photons per s, which is significantly lower than the optical saturation limit for FPs ($\sim 10^8$ excitation-photons per s). As a result, the population in the S_1 electronic state was treated under a steady state approximation. At such low irradiances, we assume minimal absorption from the dark states and therefore consider the reverse dark-state conversion to be negligible.[53] The timescales of permanent photobleaching are significantly longer than that of dark-state lifetime (ESI,† Section S4), hence it was neglected in this scheme. Incorporating these assumptions, we arrive at eqn (1) and (2) to calculate k_{DSC} and k_{GSR} for FusionRed and FusionRed-MQ,[65] and the calculated values are presented in Table 1 and Fig. 4.

$$\tau_{ON} = \frac{k_r + k_{nr} + k_{DSC}}{k_{ex} \cdot k_{dsc}} \quad (1)$$

$$\tau_{OFF} = \frac{1}{k_{GSR}} \quad (2)$$

The predictions of the simulations accurately represent experiments, where data from three independent trials revealed a hyperbolic dependence of the τ_{ON} of FusionRed and FusionRed-MQ on the excitation rates. The τ_{OFF} for both FPs showed little or no dependence on excitation rates as summarized in Table 2 and Fig. 5.

The k_{DSC} and k_{GSR} remain consistent under the range of irradiances probed in this study. However, FusionRed clearly shows a $\sim 30\%$ larger value of k_{GSR} than FusionRed-MQ, as demonstrated by a two-tailed independent t-test ($p = 0.05$) and presented in ESI,† Section S6.

Simulating ensemble behavior

We first generated normalized sum fluorescence traces for $\sim 10^3$–10^4 simulated blinking single FP trajectories using the average k_{DSC} and k_{GSR} from the single molecule experiments. The simulations indicated a larger dark fraction for FusionRed-MQ in comparison to FusionRed. We then performed simulations to obtain normalized sum fluorescence traces for blinking single FP trajectories (3 sets of 150 emitters each) by varying one rate constant at a time, including k_{Ex}, k_{DSC} and k_{GSR}. The results

Table 1 Estimation of k_{DSC} and k_{GSR}. I_N represents the irradiance measured at normal excitation. The value of k_{Ex} is excitation rate under TIRF illumination calculated respective I_N values. Details of the calculation are presented in ESI Section S2

FusionRed				FusionRed-MQ			
I_N (W cm^{-2})	k_{Ex} (s^{-1})	k_{DSC} ($\times 10^3$ s^{-1})	k_{GSR} (s^{-1})	I_N (W cm^{-2})	k_{Ex} (s^{-1})	k_{DSC} ($\times 10^3$ s^{-1})	k_{GSR} (s^{-1})
0.50	950	55 ± 11	0.19 ± 0.02	0.50	1600	52 ± 4	0.16 ± 0.02
0.63	1200	50 ± 5	0.21 ± 0.03	0.75	2400	48 ± 15	0.15 ± 0.01
0.75	1400	60 ± 7	0.19 ± 0.01	1	3300	46 ± 5	0.16 ± 0.01
1	1900	67 ± 10	0.21 ± 0.03	1.5	5200	40 ± 6	0.15 ± 0.01
3	6000	39 ± 10	0.19 ± 0.04	3	10 400	36 ± 10	0.15 ± 0.02
6	12 000	39 ± 16	0.18 ± 0.03				

This journal is © the Owner Societies 2022

Phys. Chem. Chem. Phys., 2022, **24**, 14310–14323 | **14315**
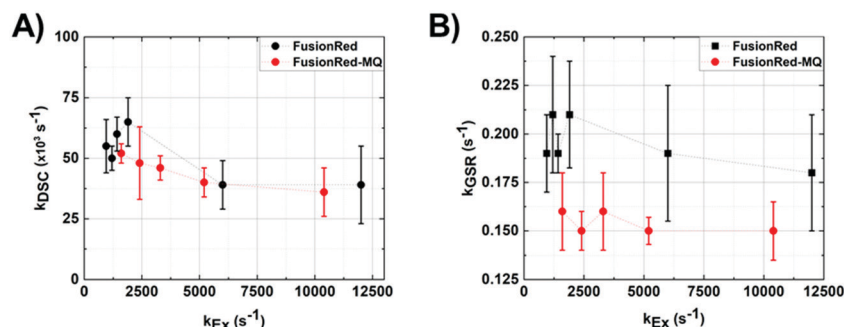
Fig. 4 Variation of rate constants (A) k_{DSC} and (B) k_{GSR} with respect to excitation rate k_{Ex} measured from single-molecule blinking experiments. The error bars indicate standard deviation errors calculated from measured τ_{OFF} and τ_{ON}.

Table 2 Experimental values of τ_{ON} and τ_{OFF}. I_N represents the irradiance measured at normal excitation. The value of k_{Ex} is excitation rate under TIRF illumination calculated respective I_N values. Details of the calculation are presented in ESI Section S2

FusionRed				FusionRed-MQ			
I_N (W cm^{-2})	k_{Ex} (s^{-1})	τ_{ON} (s)	τ_{OFF}(s)	I_N (W cm^{-2})	k_{Ex} (s^{-1})	τ_{ON} (s)	τ_{OFF} (s)
0.50	950	10.9 ± 2.3	5.3 ± 0.5	0.50	1600	4.9 ± 0.3	6.4 ± 1.5
0.63	1200	9.5 ± 1.1	4.7 ± 1	0.75	2400	3.5 ± 1.1	6.6 ± 0.5
0.75	1400	6.2 ± 0.9	5.2 ± 0.2	1	3300	2.8 ± 0.3	6.1 ± 0.1
1	1900	4.4 ± 0.4	4.8 ± 0.7	1.5	5200	2.0 ± 0.3	6.5 ± 0.5
3	6000	2.6 ± 0.5	5.3 ± 1.2	3	10 400	1.3 ± 0.4	6.5 ± 1.0
6	12 000	1.2 ± 0.5	5.8 ± 0.8				

indicated that the dark fraction increases with increasing k_{Ex} and k_{DSC} but has no or little dependence on k_{GSR} in the vicinity of measured values in the single molecule blinking experiments. This observation encouraged us to pursue an alternate analysis compared to single molecule experiments, to quantify the k_{DSC}. The results of these simulations are presented in ESI,† Section S5(e–g). The normalized fluorescence signals are proportional to the normalized population of FPs on the ground state S_0, thus the fractions of FPs on S_0 and dark state D as a function of time can be estimated as shown in ESI,† Fig. S5.7 and S8.

Ensemble photobleaching

E. coli expressing FusionRed and FusionRed-MQ were exposed to normalized widefield excitation. The decay profiles of both FPs were recorded and fit with a biexponential function as presented in ESI,† Section S4. Based on our previously reported pulsed photobleaching measurements, we assigned the slower decay component to permanent photobleaching and the faster component to reversible photobleaching due to dark-state conversion.[53] Experimental results showed a larger dark fraction for FusionRed-MQ compared to FusionRed.

To extract k_{DSC}, we consider a three-state model to represent the kinetic processes of a fluorescent protein in the first five seconds of a photobleaching trace, where the contribution of the permanent bleaching component is minimal (<10%) and reverse dark-state conversion (D to S_1) can be ignored. The rate

equations can be written in the matrix form, $\frac{d\boldsymbol{n}}{dt} = A\boldsymbol{n}$, as explicitly shown in eqn (3), where n is the population for each state (Fig. 5).

$$\frac{d}{dt}\begin{bmatrix} n_{S0} \\ n_{S1} \\ n_D \end{bmatrix} = \begin{bmatrix} -k_{Ex} & k_r + k_{nr} & k_{GSR} \\ k_{Ex} & -(k_r + k_{nr} + k_{DSC}) & 0 \\ 0 & k_{DSC} & -k_{GSR} \end{bmatrix}\begin{bmatrix} n_{S0} \\ n_{S1} \\ n_D \end{bmatrix} \quad (3)$$

The analytical solutions can be obtained by solving the eigenvalues and eigenvectors for rate equations (ESI,† Section S7). The observed fluorescence is proportional to the population in S_0 for an ensemble measurement. The resolution of the single molecule measurement in the time domain is limited by the camera acquisition time and is significantly larger than the τ_{DSC}, but smaller than the τ_{GSR}. Thus, our single molecule measurements provide an accurate estimation of the k_{GSR}, but not the k_{DSC}. Therefore, we utilize the k_{GSR} values from the single molecule measurements to fit the reversible bleaching curves of the ensemble measurements to extract a better estimation for the k_{DSC} across an irradiance range relevant to our single molecule measurements. The fluorescence decay data was fit to the analytical expression of n_{S0} to get k_{DSC} values (bound k_{GSR}). The fitting results and the estimated k_{DSC} values are provided in Fig. 6 and Table 3. While there seems to be minimal light-driven behavior for k_{DSC} for FusionRed, fitting revealed a minor (1-1.5-fold) uptick of the k_{DSC} with ~4-fold increase excitation rates for FusionRed-MQ.

Discussion

Conventional models to characterize stochastic blinking usually rely on a two-state "on" and "off" system,[28,52] when the excitation rate is much higher than the sampling rate of the detector used.[66,67] When modeling single molecule blinking with such frameworks under these conditions, one can assume emission takes place when the emitter is in the fluorescent (S_0) state for two consecutive simulation time steps ($\ll$ dark state lifetime). Imaging methods such as widefield and TIRF ($\sim 10^2$–10^6 photons per s) employ low excitation rates for SMLM schemes. In such cases, excitation and fluorescence photons
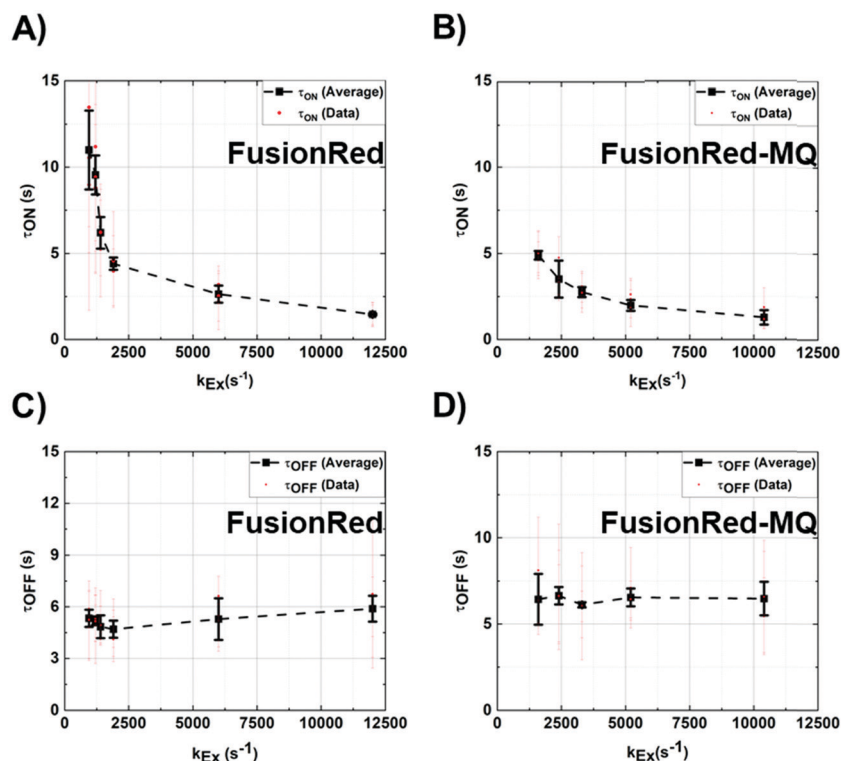
14316 | *Phys. Chem. Chem. Phys.*, 2022, **24**, 14310–14323

This journal is © the Owner Societies 2022

Fig. 5 Results from single molecule blinking experiments: Measured τ_{ON} with respect to excitation rate for (A) FusionRed and (B) FusionRed-MQ; and measured τ_{ON} with respect to excitation rate for (C) FusionRed and (D) FusionRed-MQ. The black data points are the mean $\tau_{ON/OFF}$ extracted from three independent experiments (error bars indicate the confidence intervals for the values extracted from fits).
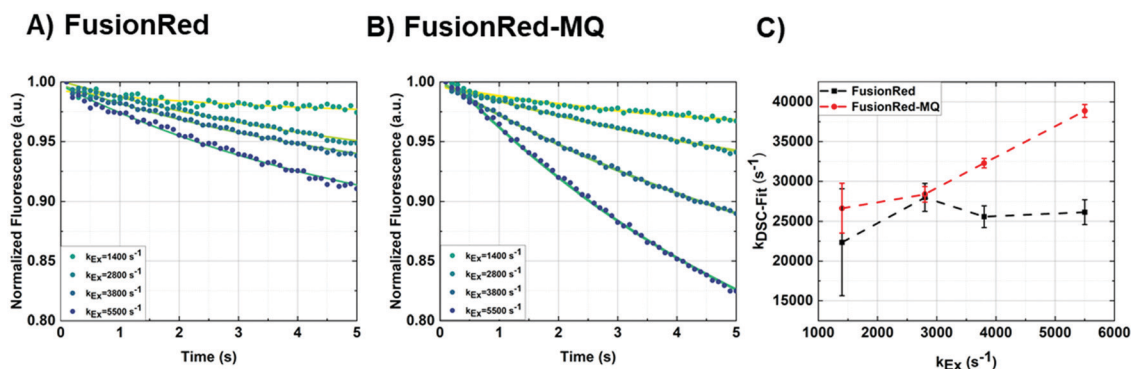

Fig. 6 Photobleaching fits from a three-state model for (A) FusionRed and (B) FusionRed-MQ, across varying irradiance ranges. (C) k_{DSC} obtained from fits. Details of the fit are provided in ESI,† Section S7. The error-bars indicate the uncertainty values for the fit.

Table 3 Estimated k_{DSC} values from fitting ensemble traces

Excitation rate (s^{-1})	k_{DSC} ($\times 10^3$ s^{-1})	
	FusionRed	FusionRed-MQ
1400	22.3 ± 6.7	26.6 ± 3.1
2800	27.9 ± 1.8	28.4 ± 0.9
3800	25.6 ± 1.4	32.3 ± 0.6
5500	26.1 ± 1.6	38.9 ± 0.8

are infrequent and long photon acquisition times are required to quantify blinking of FPs. Therefore, the detector is blind to

the molecule entering or exiting the S_1 state, and needs to be modeled differently. To address this, we devised an algorithm incorporating Monte Carlo methods with acquisition time steps longer than excited-state lifetime but shorter than τ_{GSR} (~ 100 ms). This algorithm accurately represents our single molecule experiments, where excitation rates and acquisition timescales are comparable. With this simulation algorithm, it is reasonable to assume that one always observes the FP in S_0 or D, and S_1 is only rarely populated in our three-state model. The fluorophore starts from S_0 or D and returns to these states in each time cycle, and the probability of a state change in each

This journal is © the Owner Societies 2022

Phys. Chem. Chem. Phys., 2022, **24**, 14310–14323 | **14317**

cycle is determined by rate constants of radiative emission, internal conversion, DSC and GSR processes. Our simulation of single molecule fluorescence correctly predicted the τ_{ON} dependence on k_{Ex} and k_{DSC}, and the τ_{OFF} dependence on k_{GSR}. By repeating multiple cycles of single molecule simulations, the average τ_{ON} and τ_{OFF} can be obtained based on a probability density function of an exponential distribution: $f(t) = \frac{1}{\mu} e^{-t/\mu}$ (ESI,† Section S5a–d). The model was then extended to mimic ensemble behavior (ESI,† Section S5e–g). When varying one rate constant at a time, the ensemble dark fraction increases with increasing k_{Ex} and k_{DSC}, but the fluorescence decay profile shows minor variation in dark fraction even with 30–45% variation in k_{GSR}. In other words, the dark fraction is controlled by factors affecting processes that populate the dark state, and the rate-determining ground state recovery process dominates the time constant of the faster component of decay in the fluorescence bleaching profile. Thus, simulations in both single molecule and ensemble average of RFPs qualitatively validated this three-state model.

We then developed a new method combining single molecule imaging and ensemble photobleaching measurements of RFPs with low irradiances to quantitatively extract dark state kinetic parameters based on the three-state model. The lowest irradiance in our single molecule measurements corresponds to an excitation rate of ∼1000 photons per s. At such low irradiances, we expect an emission of less than 100 photons per frame from the dimmer FusionRed (ESI,† Section S9). The relatively long τ_{ON} and low intensity-change thresholds for on to off (or *vice versa*) state changes pose a challenge for data analysis under these conditions. For these low irradiances, conventional algorithms to binarize intensity traces inaccurately binarize on and off events due to the low signal to noise ratios. Thresholding a change of state, in particular is a challenging step.[61,68] Instead, we used algorithms based on statistics of intensity variation across frames to predict possible state change points and determine if a "real" on to off (or *vice versa*) event takes place.[68] The analysis algorithm is also helpful to predict very short τ_{ON} for the other extreme case where we use ∼10-fold higher excitation rates. Outside sample preparation methods and efficient data analysis algorithms, experimental analysis of such discrete states can also be improved with improved camera technologies like photon-number resolving detections schemes.[69] Additionally, to accurately determine on and off events, our algorithm screened out instances where two molecules might fluoresce at the same time or the molecule undergoes permanent photobleaching or denatures (extracts τ_{OFF} only when the event is bounded by an on time and *vice versa*). Moreover, it is worth noting that the blinking rates are sensitive to the nature of the electrostatic interaction between the binding surface and the molecule. Glass surfaces under treatments like exposure to plasma are generally negatively charged prompting interactions with the positively charged areas of the protein (ESI,† Section S10).[70] For example, the super-resolution imaging modality FLINC (Fluorescence fLuctuation INcrease by Contact) is based on variation of

blinking frequency in TagRFP-T (by ∼25%) through the electrostatic interaction with another non-fluorescent FP (Dronpa).[71] Assuming that FusionRed binds to the glass surface *via* positively charged surfaces facing outward from the β-barrel, we may expect these effects to be identical for FusionRed-MQ, which has only two internal mutations compared to FusionRed. Therefore, this method of sample preparation might introduce artifacts to blinking dynamics in the context of comparing two FPs with dissimilar residues facing out of the β barrel structure.

Our data analysis algorithms revealed computed rate constants k_{DSC} and k_{GSR} obtained from τ_{ON} and τ_{OFF} histograms, had minimal variation in the irradiance regimes examined for both FPs. The value of k_{GSR} can be accurately determined from the single molecule fluorescence dynamics because the time resolution of the measurement, which is limited by the camera acquisition time, is smaller than the τ_{GSR}. Therefore, we conclusively determined that the k_{GSR} for FusionRed is 1.3-fold higher than that of FusionRed-MQ. Additional statistical testing indicated that these results were statistically significant. (ESI,† Section S6). We also verified our hypothesis that k_{GSR} of both FPs is independent of k_{Ex} under low irradiances. The k_{DSC} values are, however, on the order of kHz, which is ∼2 orders of magnitude larger than the acquisition rate (Hz) of our single-molecule experiment. While the k_{DSC} values are in the range of expected values from previous measurements, and despite high precision, accurate values of k_{DSC} under low irradiances had to be determined by a different method. We used an eigenvector-eigenvalue approach to extract analytical expressions for fluorescence decay from the kinetics of our three-state model and fit ensemble biexponential bleaching traces to estimate the k_{DSC} with a higher accuracy. The fitting analysis revealed a light-driven dependency for the k_{DSC} (∼1.5-fold increase in the k_{DSC} with ∼4-fold increase in the k_{Ex}) of FusionRed-MQ, whereas k_{DSC} of FusionRed remained almost constant with increasing excitation rate. Although a degree of variability can be expected between single-molecule measurements on purified proteins in buffer and ensemble measurements in the bacterial cytoplasm, from the biochemical point of view it is encouraging to note that FusionRed has low pH sensitivity in the neutral pH range and the pH values of our imaging buffer and bacterial cytoplasm are similar (∼7.4 *vs.* ∼7.2–7.8 for *E. coli*).[72]

The increase of the k_{DSC} with the k_{Ex} for FusionRed-MQ is not an intuitive observation. We only observe a ∼3-fold drop in the τ_{ON} for a ∼4-fold increase in k_{Ex} from our single molecule measurements for FusionRed-MQ (Table 2; Between 0.75 and 3 W cm^{-2}). If the increase of k_{DSC} were to be accounted for by increasing irradiances, a drop of ∼6-fold should be expected in the τ_{ON} for FusionRed-MQ. While this observation can be representative of errors in our experimental techniques, data analysis algorithms or the inability of the three-state model to accurately represent the system, it is important to note that the k_{DSC} represents the rate constant of photoconversion into a dark form, usually within the excited state manifold. At high irradiances, a increase irradiance can translate to increments in the local temperature. This can accelerate the k_{DSC} based on an

14318 | *Phys. Chem. Chem. Phys.*, 2022, **24**, 14310–14323

This journal is © the Owner Societies 2022

Arrhenius-like behavior, which we previously noted for measurements to quantify k_{DSC} within RFPs mCherry, Kreik and TagRFP-T.[64] However, the independence of k_{DSC} on k_{Ex} for FusionRed (with 2-fold larger internal conversion rate constant) rules out this possibility. FusionRed shows $\sim$9-fold drop in the τ_{ON} for a $\sim$10-fold increase in k_{Ex}, consistent with the model where k_{DSC} is fairly constant across a low irradiance regime. On the other hand, from a catalytic perspective, an increase of k_{DSC} with irradiance can indicate a drop in a barrier height to cross over to a dark form or possible access to other dark states through independent mechanisms. As discussed previously, through-space interactions between closely spaced FPs Dronpa and TagRFP-T change blinking rates for TagRFP-T, which resulted in the discovery of the super-resolution imaging modality FLINC.[71] Since our approach to extract a k_{DSC} involves combining a single-molecule and an ensemble experiment – it is possible that in our ensemble measurement, FPs in close proximity potentially impact each other's dark state conversion pathways. Moreover, dark state conversion pathways are sensitive to the electronic distribution on and around the chromophore.[73] FusionRed-MQ involves the substitution of non-polar Met42 to the polar Gln, and as we discuss in the preceding sections – both electrostatics and sterics have roles to play in ground and excited state photo-isomerization processes, which possibly control access to dark states.[73] In other words, the k_{DSC} obtained from fitting the over-simplified three-state model could be an effective k_{DSC} with multiple irradiance-dependent competing dark state conversion processes. Higher time-resolution measurements of the dark state kinetics might provide further insights into the mechanisms of the dark state conversion process in FusionRed-MQ, which currently lie beyond the scope of this study.

Next, we consider the photophysics in the context of protein structure. The crystal structure shows that Met residue at position 42 in FusionRed is located at the imidazolinone end of the chromophore ($\sim$3 Å). In FusionRed-MQ position 42 is substituted for a Gln residue, possibly altering the hydrogen bonding patterns at the acylimine end of the chromophore.[53] Meanwhile, the residue at position 175 located above the phenol ring of the chromophore pocket; is a Leu in FusionRed

and is substituted to the larger sidechain Met in FusionRed-MQ.[53,56,74] As reported in our previous work, crystal structure data indicates that the residue L175 in FusionRed is approximately 5 Å from the phenol ring of the chromophore.[53] The effects of these two mutations on FusionRed's brightness are complementary. Unlike the C159V mutation, M42Q and L175M do not change the profile of the ensemble bleaching, likely preserving the efficient *cis* to *trans* dark-state isomerization pathway.[53] It is interesting to note that the amino acid residue analogous to position 175 in FusionRed influences the dark-state behavior of the two photoconvertible FPs IrisFP and mEos4B (S173 *vs.* F173).[38] De-Zitter and co-workers demonstrated that F173 in mEos4B reduced the number of hydrogen bonds maintained by the dark chromophore in its green form compared to the smaller-sized but hydrogen-bonding capable S173 residue for IrisFP, providing an explanation for the reduced photoswitching contrast.[38] As such, the k_{GSR} values can help to identify a possible difference in barrier for dark to fluorescent state interconversion (Fig. 7) between FusionRed and FusionRed-MQ. The approximate difference in the ground state barrier of bond rotation expected for a *trans* to *cis* isomerization can be calculated using a *trans*ition state theory approach for interconverting ground state isomers. Under the assumption that the local temperature does not change on irradiation and a similar value of the pre-exponential factor, this difference in barrier ($\Delta\Delta G^{\#}$) is $\sim$20 kJ mol^{-1} for FusionRed and FusionRed-MQ. A value of 20 kJ mol^{-1} is a reasonable free energy difference that predicts a change of a few possible hydrogen bonds, similar to what was observed for IrisFP, mEos4B and others.[38,75–78]

Furthermore, the isomerization coordinates of the bonds bridging the phenol (P-bond) and imidazolinone (I-bond) rings of the FP chromophore to the methine carbon impact the molecular brightness of a fluorescent protein molecule.[79] Recent studies on anionic GFP and RFP chromophores have suggested both electrostatics and sterics play important roles in the rotation of the P and the I-bonds for the ground and the excited electronic states.[80,81] These isomerization coordinates often control access to ultrafast non-radiative relaxation channels, such as population loss in RFPs on fluorescent state
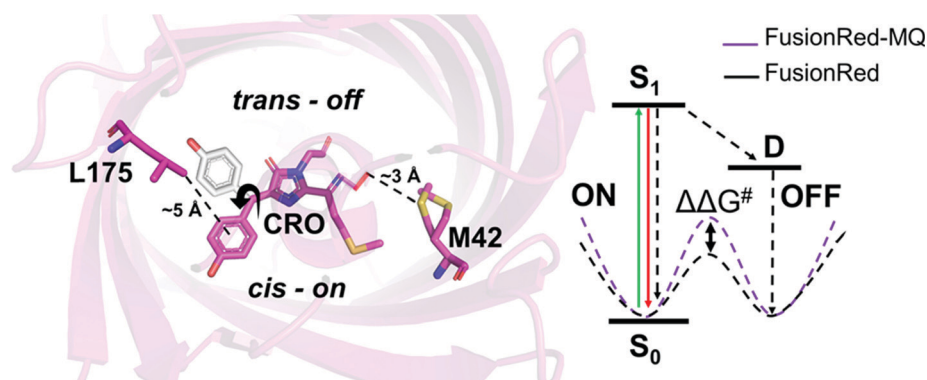

Fig. 7 (Left) The spatial orientation of the L175 and M42 residues in the FusionRed crystal structure (PDB ID: 6U1A), with the *cis* and the trans forms of the chromophore. (Right) Schematic depiction of a possible barrier for a ground state *cis*–*trans* isomerization depicting a switch from an off to an on state.

This journal is © the Owner Societies 2022

Phys. Chem. Chem. Phys., 2022, **24**, 14310–14323 | **14319**

through a conical intersection seam regulated by access to twisted intramolecular charge transfer (TICT) states.[82] Directed evolution of fluorescence lifetime on mCherry revealed mutations at four positions near the phenol end of the chromophore can result in a 3-fold increment in fluorescence quantum yield – most likely through a combination of steric and electrostatic effects.[83] One can foresee the impact on sterics by the substitution of a Leu residue with a longer Met residue ($\sim$4 vs. 3-single linear bonds) at position 175. Simultaneously, the substitution of the non-polar Met sidechain to the similar sized polar Gln sidechain at position 42 may impact pathways of electron-flow across the chromophore, highly sensitive to electrostatics. Therefore, an energetic reluctance to switch back to the bright state can be explained by a conformationally restricted chromophore for FusionRed-MQ, additionally suggesting a mechanism for the $\sim$2-fold higher brightness observed for the FusionRed-L175M M42Q variant.[53,74]

Conclusions

Bright RFPs with desirable biological properties have a growing role as strong candidates for dual-usage both for SMLM-based imaging and widefield ensemble assays.[51] To address the latter, in this study we quantified the nature and timescales of dark state conversion and ground state recovery for FusionRed and its 2.5-fold brighter progeny FusionRed-MQ. Our approach combined single molecule imaging with ensemble bleaching measurements to extract k_{DSC} and k_{GSR} of these RFPs. The methods applied in this work are an advancement over our and other previous studies where rate constants were extracted using time and frequency domain measurements at several orders of magnitude higher irradiances, which are often not suitable for widefield fluorescence and SMLM-based imaging assays.[64] To the best of our knowledge, this is the first study to quantify k_{DSC} and k_{GSR} directly under low irradiances relevant to modern SMLM imaging schemes like SOFI. We verified our hypothesis that k_{GSR} of FusionRed and FusionRed-MQ is independent of k_{Ex} under low irradiances. This is contrary to high irradiance studies where k_{GSR} was observed to vary with k_{Ex}.[28,52] FusionRed is a plausible candidate for SMLM imaging,[55] and our investigation suggests FusionRed-MQ is a better choice for such applications owing to its 1.8-fold higher quantum yield and higher k_{DSC} and smaller k_{GSR}.[53] The methods and results of this work can be extended to the characterization of other fluorophores with appropriate dark state kinetic models, or incorporated into multi-parametric screening technologies to select FPs with high rates of blinking for imaging methods such as SOFI.

Author contributions

S. T. H., S. M. and R. J. conceptualized the study. S. M., S. T. H. and E. S. designed and performed the experiments. S. M., C. T., S. T. H, and R. W., developed data analysis methods in the study. S. M., R. J., S. T. H. and C. T. wrote the manuscript.

Conflicts of interest

The authors declare no competing financial interests.

Acknowledgements

References

1 A. D. Elliott, Confocal Microscopy: Principles and Modern Practices, *Curr. Protoc. Cytom.*, 2020, **92**, e68.

2 A. Ahmed, J. Schoberer, E. Cooke and S. W. Botchway, in *Methods in Molecular Biology*, ed. A. Poterszman, Springer US, New York, NY, 2021, vol. 2247, pp. 287–301.

3 H. M. Schouw, L. A. Huisman, Y. F. Janssen, R. H.-J. A. Slart, R. J.-H. Borra, A. T.-M. Willemsen, A. H. Brouwers, J. M. van Dijl, R. A. Dierckx, G. M. van Dam, W. Szymanski, H. H. Boersma and S. Kruijff, Targeted optical fluorescence imaging: a meta-narrative review and future perspectives, *Eur. J. Nucl. Med. Mol. Imaging*, 2021, **48**, 4272–4292.

4 R. Datta, T. M. Heaster, J. T. Sharick, A. A. Gillette and M. C. Skala, Fluorescence lifetime imaging microscopy: fundamentals and advances in instrumentation, analysis, and applications, *J. Biomed. Opt.*, 2020, **25**, 1.

5 W. R. Algar, N. Hildebrandt, S. S. Vogel and I. L. Medintz, FRET as a biomolecular research tool — understanding its potential while avoiding pitfalls, *Nat. Methods*, 2019, **16**, 815–829.

6 S. Duwé and P. Dedecker, Optimizing the Fluorescent Protein Toolbox and Its Use, *Curr. Opin. Biotechnol*, 2019, **58**, 183–191.

7 G. Breuer, A formal representation of abbe's theory of microscopic image formation, *Opt. Acta*, 1984, **31**, 661–670.

8 J. Chojnacki and C. Eggeling, Super-resolution fluorescence microscopy studies of human immunodeficiency virus, *Retrovirology*, 2018, **15**, 41.

14320 | *Phys. Chem. Chem. Phys.*, 2022, **24**, 14310–14323

This journal is © the Owner Societies 2022

9   J. Vangindertael, R. Camacho, W. Sempels, H. Mizuno, P. Dedecker and K. P.-F. Janssen, An introduction to optical super-resolution microscopy for the adventurous biologist, *Methods Appl. Fluoresc.*, 2018, **6**, 22003.

10 A. S. Mishin and K. A. Lukyanov, Live-Cell Super-resolution Fluorescence Microscopy, *Biochemistry*, 2019, **84**, 19–31.

11 L. Schermelleh, A. Ferrand, T. Huser, C. Eggeling, M. Sauer, O. Biehlmaier and G. P.-C. Drummen, Super-resolution microscopy demystified, *Nat. Cell Biol.*, 2019, **21**, 72–84.

12 L. Chen, X. Chen, X. Yang, C. He, M. Wang, P. Xi and J. Gao, Advances of super-resolution fluorescence polarization microscopy and its applications in life sciences, *Comput. Struct. Biotechnol. J.*, 2020, **18**, 2209–2216.

13 V. Schubert, P. Neumann, A. Marques, S. Heckmann, J. Macas, A. Pedrosa-Harand, I. Schubert, T.-S. Jang and A. Houben, Super-Resolution Microscopy Reveals Diversity of Plant Centromere Architecture, *Int. J. Mol. Sci.*, 2020, **21**, 3488.

14 S. W. Hell and J. Wichmann, Breaking the diffraction resolution limit by stimulated emission: stimulated-emission-depletion fluorescence microscopy, *Opt. Lett.*, 1994, **19**, 780.

15 E. Betzig, G. H. Patterson, R. Sougrat, O. W. Lindwasser, S. Olenych, J. S. Bonifacino, M. W. Davidson, J. Lippincott-Schwartz and H. F. Hess, Imaging intracellular fluorescent proteins at nanometer resolution, *Science*, 2006, **313**, 1642–1645.

16 W. E. Moerner, Microscopy beyond the diffraction limit using actively controlled single molecules, *J. Microsc.*, 2012, **246**, 213–220.

17 L. Möckl and W. E. Moerner, Super-resolution Microscopy with Single Molecules in Biology and Beyond-Essentials, Current Trends, and Future Challenges, *J. Am. Chem. Soc.*, 2020, **142**, 17828–17844.

18 T. Dertinger, R. Colyera, G. Iyer, S. Weiss and J. Enderlein, Fast, background-free, 3D super-resolution optical fluctuation imaging (SOFI), *Proc. Natl. Acad. Sci. U. S. A.*, 2009, **106**, 22287–22292.

19 P. D. Simonson, E. Rothenberg and P. R. Selvin, Single-molecule-based super-resolution images in the presence of multiple fluorophores, *Nano Lett.*, 2011, **11**, 5090–5096.

20 D. T. Burnette, P. Sengupta, Y. Dai, J. Lippincott-Schwartz and B. Kachar, Bleaching/blinking assisted localization microscopy for superresolution imaging using standard fluorescent molecules, *Proc. Natl. Acad. Sci. U. S. A.*, 2011, **108**, 21081–21086.

21 P. D. Dahlberg, S. Saurabh, A. M. Sartor, J. Wang, J. Wang, P. G. Mitchell, W. Chiu, W. Chiu, L. Shapiro and W. E. Moerner, Cryogenic single-molecule fluorescence annotations for electron tomography reveal in situ organization of key proteins in Caulobacter, *Proc. Natl. Acad. Sci. U. S. A.*, 2020, **117**, 13937–13944.

22 M. Lelek, M. T. Gyparaki, G. Beliu, F. Schueder, J. Griffié, S. Manley, R. Jungmann, M. Sauer, M. Lakadamyali and C. Zimmer, Single-molecule localization microscopy, *Nat. Rev. Methods Primers*, 2021, **1**, 39.

23 W. Vandenberg, M. Leutenegger, S. Duwé and P. Dedecker, An Extended Quantitative Model for Super-Resolution Optical Fluctuation Imaging (SOFI), *Opt. Express*, 2019, **27**(18), 25749.

24 R. van den Eynde, A. Sandmeyer, W. Vandenberg, S. Duwé, W. Hübner, T. Huser, P. Dedecker and M. Müller, Quantitative comparison of camera technologies for cost-effective super-resolution optical fluctuation imaging (SOFI), *JPhys Photonics*, 2019, **1**, 44001.

25 B. Moeyaert, W. Vandenberg and P. Dedecker, SOFIevaluator: a strategy for the quantitative quality assessment of SOFI data, *Biomed. Opt. Express*, 2020, **11**, 636.

26 R. M. Dickson, A. B. Cubitt, R. Y. Tsient and W. E. Moerner, On/off blinking and switching behaviour of single molecules of green fluorescent protein, *Nature*, 1997, **388**, 355–358.

27 M. F. Garcia-Parajo, G. M.-J. Segers-Nolten, J. A. Veerman, J. Greve and N. F. Van Hulst, Real-time light-driven dynamics of the fluorescence emission in single green fluorescent protein molecules, *Proc. Natl. Acad. Sci. U. S. A.*, 2000, **97**, 7237–7242.

28 P. Schwille, S. Kummer, A. A. Heikal, W. E. Moerner and W. W. Webb, Fluorescence correlation spectroscopy reveals fast optical excitation-driven intramolecular dynamics of yellow fluorescent proteins, *Proc. Natl. Acad. Sci. U. S. A.*, 2000, **97**, 151–156.

29 F. Malvezzi-Campeggi, M. Jahnz, K. G. Heinze, P. Dittrich and P. Schwille, Light-induced flickering of DsRed provides evidence for distinct and interconvertible fluorescent states, *Biophys. J.*, 2001, **81**, 1776–1785.

30 M. F. Garcia-Parajo, M. Koopman, E. M.-H. P. Van Dijk, V. Subramaniam and N. F. Van Hulst, The nature of fluorescence emission in the red fluorescent protein DsRed, revealed by single-molecule detection, *Proc. Natl. Acad. Sci. U. S. A.*, 2001, **98**, 14392–14397.

31 U. Haupts, S. Maiti, P. Schwille and W. W. Webb, Dynamics of fluorescence fluctuations in green fluorescent protein observed by fluorescence correlation spectroscopy, *Proc. Natl. Acad. Sci. U. S. A.*, 1998, **95**, 13573–13578.

32 A. A. Heikal, S. T. Hess, G. S. Baird, R. Y. Tsien and W. W. Webb, Molecular Spectroscopy and Dynamics of Intrinsically Fluorescent Proteins: Coral Red (DsRed) and Yellow (Citrine), *Proc. Natl. Acad. Sci. U. S. A.*, 2000, **97**(22), 11996–12001.

33 D. Sinnecker, P. Voigt, N. Hellwig and M. Schaefer, Reversible photobleaching of enhanced green fluorescent proteins, *Biochemistry*, 2005, **44**, 7085–7097.

34 R. Berardozzi, V. Adam, A. Martins and D. Bourgeois, Arginine 66 Controls Dark-State Formation in Green-to-Red Photoconvertible Fluorescent Proteins, *J. Am. Chem. Soc.*, 2016, **138**, 558–565.

35 D. Thédié, R. Berardozzi, V. Adam and D. Bourgeois, Photoswitching of Green mEos2 by Intense 561 nm Light Perturbs Efficient Green-to-Red Photoconversion in Localization Microscopy, *J. Phys. Chem. Lett.*, 2017, **8**, 4424–4430.

36 E. De Zitter, D. Thédié, V. Mönkemöller, S. Hugelier, J. Beaudouin, V. Adam, M. Byrdin, L. Van Meervelt,

P. Dedecker and D. Bourgeois, Mechanistic investigation of mEos4b reveals a strategy to reduce track interruptions in sptPALM, *Nat. Methods*, 2019, **16**, 707–710.

37 T. D. Krueger, L. Tang, L. Zhu, I. L. Breen, R. M. Wachter and C. Fang, Dual Illumination Enhances Transformation of an Engineered Green-to-Red Photoconvertible Fluorescent Protein, *Angew. Chem., Int. Ed.*, 2020, **59**, 1644–1652.

38 E. De Zitter, J. Ridard, D. Thédié, V. Adam, B. Lévy, M. Byrdin, G. Gotthard, L. Van Meervelt, P. Dedecker, I. Demachy and D. Bourgeois, Mechanistic Investigations of Green mEos4b Reveal a Dynamic Long-Lived Dark State, *J. Am. Chem. Soc.*, 2020, **142**, 10978–10988.

39 A. C. Stiel, M. Andresen, H. Bock, M. Hilbert, J. Schilde, A. Schönle, C. Eggeling, A. Egner, S. W. Hell and S. Jakobs, Generation of monomeric reversibly switchable red fluorescent proteins for far-field fluorescence nanoscopy, *Biophys. J.*, 2008, **95**, 2989–2997.

40 R. Ando, H. Mizuno and A. Miyawaki, Regulated fast nucleocytoplasmic shuttling observed by reversible protein highlighting, *Science*, 2004, **306**, 1370–1373.

41 T. Grotjohann, I. Testa, M. Leutenegger, H. Bock, N. T. Urban, F. Lavoie-Cardinal, K. I. Willig, C. Eggeling, S. Jakobs and S. W. Hell, Diffraction-unlimited all-optical imaging and writing with a photochromic GFP, *Nature*, 2011, **478**, 204–208.

42 G. Donnert, C. Eggeling and S. W. Hell, Major signal increase in fluorescence microscopy through dark-state relaxation, *Nat. Methods*, 2007, **4**, 81–86.

43 D. P. Mahoney, E. A. Owens, C. Fan, J. C. Hsiang, M. M. Henary and R. M. Dickson, Tailoring Cyanine Dark States for Improved Optically Modulated Fluorescence Recovery, *J. Phys. Chem. B*, 2015, **119**, 4637–4643.

44 A. E. Jablonski, J. C. Hsiang, P. Bagchi, N. Hull, C. I. Richards, C. J. Fahrni and R. M. Dickson, Signal discrimination between fluorescent proteins in live cells by long-wavelength optical modulation, *J. Phys. Chem. Lett.*, 2012, **3**, 3585–3591.

45 Y. C. Chen, A. E. Jablonski, I. Issaeva, D. Bourassa, J. C. Hsiang, C. J. Fahrni and R. M. Dickson, Optically Modulated Photoswitchable Fluorescent Proteins Yield Improved Biological Imaging Sensitivity, *J. Am. Chem. Soc.*, 2015, **137**, 12764–12767.

46 B. C. Fleischer, J. T. Petty, J. C. Hsiang and R. M. Dickson, Optically Activated Delayed Fluorescence, *J. Phys. Chem. Lett.*, 2017, **8**, 3536–3543.

47 D. P. Mahoney, A. A. Demissie and R. M. Dickson, Optically Activated Delayed Fluorescence through Control of Cyanine Dye Photophysics, *J. Phys. Chem. A*, 2019, **123**, 3599–3606.

48 B. Peng, R. Dikdan, S. E. Hill, A. C. Patterson-Orazem, R. L. Lieberman, C. J. Fahrni and R. M. Dickson, Optically Modulated and Optically Activated Delayed Fluorescent Proteins through Dark State Engineering, *J. Phys. Chem. B*, 2021, **125**, 5200–5209.

49 S. Waldchen, J. Lehmann, T. Klein, S. Van De Linde and M. Sauer, Light-induced cell damage in live-cell super-resolution microscopy, *Sci. Rep.*, 2015, **5**, 15348.

50 P. P. Laissue, R. A. Alghamdi, P. Tomancak, E. G. Reynaud and H. Shroff, Assessing phototoxicity in live fluorescence imaging, *Nat. Methods*, 2017, **14**, 657–661.

51 S. Mukherjee and R. Jimenez, Photophysical Engineering of Fluorescent Proteins: Accomplishments and Challenges of Physical Chemistry Strategies, *J. Phys. Chem. B*, 2022, **126**, 735–750.

52 A. Schenk, S. Ivanchenko, C. Röcker, J. Wiedenmann and G. U. Nienhaus, Photodynamics of Red Fluorescent Proteins Studied by Fluorescence Correlation Spectroscopy, *Biophys. J.*, 2004, **86**, 384–394.

53 S. Mukherjee, S. T. Hung, N. Douglas, P. Manna, C. Thomas, A. Ekrem, A. E. Palmer and R. Jimenez, Engineering of a brighter variant of the FusionRed fluorescent protein using lifetime flow cytometry and structure-guided mutations, *Biochemistry*, 2020, **59**, 3669–3682.

54 W. Weber, V. Helm, J. A. Mccammon and P. W. Langhoff, Shedding light on the dark and weakly fluorescent states of green fluorescent proteins, *Proc. Natl. Acad. Sci. U. S. A.*, 1999, **96**, 6177–6182.

55 N. V. Klementieva, A. I. Pavlikov, A. A. Moiseev, N. G. Bozhanova, N. M. Mishina, S. A. Lukyanov, E. V. Zagaynova, K. A. Lukyanov and A. S. Mishin, Intrinsic blinking of red fluorescent proteins for super-resolution microscopy, *Chem. Commun.*, 2017, **53**, 949–951.

56 L. Muslinkina, V. Z. Pletnev, N. V. Pletneva, D. A. Ruchkin, D. V. Kolesov, A. M. Bogdanov, L. A. Kost, T. V. Rakitina, Y. K. Agapova, I. I. Shemyakina, D. M. Chudakov and S. Pletnev, Two independent routes of post-translational chemistry in fluorescent protein FusionRed, *Int. J. Biol. Macromol.*, 2020, **155**, 551–559.

57 F. Pennacchietti, E. O. Serebrovskaya, A. R. Faro, I. I. Shemyakina, N. G. Bozhanova, A. A. Kotlobay, N. G. Gurskaya, A. Bodén, J. Dreier, D. M. Chudakov, K. A. Lukyanov, V. V. Verkhusha, A. S. Mishin and I. Testa, Fast reversibly photoswitching red fluorescent proteins for live-cell RESOLFT nanoscopy, *Nat. Methods*, 2018, **15**, 601–604.

58 M. Honda, Y. Saito, N. I. Smith, K. Fujita and S. Kawata, Nanoscale heating of laser irradiated single gold nanoparticles in liquid, *Opt. Express*, 2011, **19**, 12375.

59 J. L. Davis, B. Dong, C. Sun and H. F. Zhang, Method to identify and minimize artifacts induced by fluorescent impurities in single-molecule localization microscopy, *J. Biomed. Opt.*, 2018, **23**, 1.

60 C. Tregidgo, J. A. Levitt and K. Suhling, Effect of refractive index on the fluorescence lifetime of green fluorescent protein, *J. Biomed. Opt.*, 2008, **13**, 031218.

61 L. P. Watkins and H. Yang, Detection of intensity change points in time-resolved single-molecule measurements, *J. Phys. Chem. B*, 2005, **109**, 617–628.

62 H. F. Ng, Automatic thresholding for defect detection, *Pattern Recognit. Lett.*, 2006, **27**, 1644–1649.

63 L. Kamentsky, T. R. Jones, A. Fraser, M. A. Bray, D. J. Logan, K. L. Madden, V. Ljosa, C. Rueden, K. W. Eliceiri and A. E. Carpenter, Improved structure, function and

14322 | *Phys. Chem. Chem. Phys.*, 2022, **24**, 14310–14323

This journal is © the Owner Societies 2022

compatibility for CellProfiler: Modular high-throughput image analysis software, *Bioinformatics*, 2011, **27**, 1179–1180.

64 P. Manna and R. Jimenez, Time and frequency-domain measurement of ground-state recovery times in red fluorescent proteins, *J. Phys. Chem. B*, 2015, **119**, 4944–4954.

65 W. T. Yip, D. Hu, J. Yu, D. A. Vanden Bout and P. F. Barbara, Classifying the photophysical dynamics of single- and multiple-chromophoric molecules by single molecule spectroscopy, *J. Phys. Chem. A*, 1998, **102**, 7564–7575.

66 E. J.-G. Peterman, S. Brasselet and W. E. Moerner, The fluorescence dynamics of single molecules of green fluorescent protein, *J. Phys. Chem. A*, 1999, **103**, 10553–10560.

67 B. Lounis, J. Deich, F. I. Rosell, S. G. Boxer and W. E. Moerner, Photophysics of DsRed, a red fluorescent protein, from the ensemble to the single-molecule level, *J. Phys. Chem. B*, 2002, **105**, 5048–5054.

68 H. Yang, H. Li and T. Liu, Photobleaching statistics in single-molecule on-/off-time distributions, *J. Chem. Phys.*, 2019, **151**, 174101.

69 L. Qi, F. Just, G. Leuchs and M. V. Chekhova, Autonomous absolute calibration of an ICCD camera in single-photon detection regime, *Opt. Express*, 2016, **24**, 26444.

70 S. H. Behrens and D. G. Grier, The charge of glass and silica surfaces, *J. Chem. Phys.*, 2001, **115**, 6716–6721.

71 G. C.-H. Mo, B. Ross, F. Hertel, P. Manna, X. Yang, E. Greenwald, C. Booth, A. M. Plummer, B. Tenner, Z. Chen, Y. Wang, E. J. Kennedy, P. A. Cole, K. G. Fleming, A. Palmer, R. Jimenez, J. Xiao, P. Dedecker and J. Zhang, Genetically encoded biosensors for visualizing live-cell biochemical activity at super-resolution, *Nat. Methods*, 2017, **14**, 427–434.

72 J. C. Wilks and J. L. Slonczewski, pH of the cytoplasm and periplasm of Escherichia coli: Rapid measurement by green fluorescent protein fluorimetry, *J. Bacteriol.*, 2007, **189**, 5601–5607.

73 C. Y. Lin, M. G. Romei, I. I. Mathews and S. G. Boxer, Energetic Basis and Design of Enzyme Function Demonstrated Using GFP, an Excited-State Enzyme, *J. Am. Chem. Soc.*, 2022, **144**, 3968–3978.

74 P. Manna, S. T. Hung, S. Mukherjee, P. Friis, D. M. Simpson, M. N. Lo, A. E. Palmer and R. Jimenez, Directed evolution of excited state lifetime and brightness in FusionRed using a microfluidic sorter, *Integr. Biol.*, 2018, **10**, 516–526.

75 X. He, A. F. Bell and P. J. Tonge, Ground state isomerization of a model green fluorescent protein chromophore, *FEBS Lett.*, 2003, **549**, 35–38.

76 S. Rafiq, B. K. Rajbongshi, N. N. Nair, P. Sen and G. Ramanathan, Excited state relaxation dynamics of model green fluorescent protein chromophore analogs: Evidence for *cis–trans* isomerism, *J. Phys. Chem. A*, 2011, **115**, 13733–13742.

77 E. Carrascosa, J. N. Bull, M. S. Scholz, N. J.-A. Coughlan, S. Olsen, U. Wille and E. J. Bieske, Reversible Photoisomerization of the Isolated Green Fluorescent Protein Chromophore, *J. Phys. Chem. Lett.*, 2018, **9**, 2647–2651.

78 J. Chang, M. G. Romei and S. G. Boxer, Structural Evidence of Photoisomerization Pathways in Fluorescent Proteins, *J. Am. Chem. Soc.*, 2019, **141**, 15504–15508.

79 N. H. List, C. M. Jones and T. J. Martínez, Internal conversion of the anionic GFP chromophore: In and out of the I-twisted S1/S0 conical intersection seam, *Chem. Sci.*, 2022, **13**, 373–385.

80 C. Y. Lin, M. G. Romei, L. M. Oltrogge, I. I. Mathews and S. G. Boxer, Unified Model for Photophysical and Electro-Optical Properties of Green Fluorescent Proteins, *J. Am. Chem. Soc.*, 2019, **141**, 15250–15265.

81 M. G. Romei, C. Y. Lin, I. I. Mathews and S. G. Boxer, Electrostatic control of photoisomerization pathways in proteins, *Science*, 2020, **367**, 76–79.

82 M. Drobizhev, R. S. Molina, P. R. Callis, J. N. Scott, G. G. Lambert, A. Salih, N. C. Shaner and T. E. Hughes, Local Electric Field Controls Fluorescence Quantum Yield of Red and Far-Red Fluorescent Proteins, *Front. Mol. Biosci.*, 2021, **8**, 633217.

83 S. Mukherjee, P. Manna, S. T. Hung, F. Vietmeyer, P. Friis and A. Palmer, *et al.*, Directed evolution of a bright variant of mCherry: Suppression of non-radiative decay by fluorescence lifetime selections, *J. Phys. Chem. B*, 2022, Accepted (ChemRxiv: DOI: **10.26434/chemrxiv-2022-v3t03**).

This journal is © the Owner Societies 2022

Phys. Chem. Chem. Phys., 2022, **24**, 14310–14323 | **14323**